




Communication

# CeO<sub>2</sub>-Azacrown Conjugate as a Nanoplatfor for Combined Radiopharmaceuticals

Sofia Khabirova <sup>1,\*</sup> , Gleb Aleshin <sup>1</sup> , Tatiana Plakhova <sup>1</sup>, Anastasia Zubenko <sup>2</sup>, Anna Shchukina <sup>2</sup> , Olga Fedorova <sup>2</sup>, Aleksey Averin <sup>3</sup>, Ekaterina Belova <sup>1</sup>, Elena Bazarkina <sup>4,5</sup>, Kristina Kvashnina <sup>4,5</sup> and Stepan Kalmykov <sup>1</sup>

<sup>1</sup> Department of Chemistry, Lomonosov Moscow State University, Leninskie Gory, 1/3, 119991 Moscow, Russia

<sup>2</sup> N. Nesmeyanov Institute of Organoelement Compounds of Russian Academy of Sciences, Vavilova, 28, GSP-1, 119991 Moscow, Russia

<sup>3</sup> Frumkin Institute of Physical Chemistry and Electrochemistry Russian Academy of Sciences, Leninskiy Ave. 31b4, 119991 Moscow, Russia

<sup>4</sup> The Rossendorf Beamline at ESRF—The European Synchrotron, CS40220, CEDEX 9, 38043 Grenoble, France

<sup>5</sup> Helmholtz Zentrum Dresden-Rossendorf (HZDR), Institute of Resource Ecology, P.O. Box 510119, 01314 Dresden, Germany

\* Correspondence: khabirovasophia@gmail.com; Tel.: +7-9661919972

**Abstract:** This study is one of the first attempts to assess CeO<sub>2</sub> nanoparticles as a nanoplatfor for radiopharmaceuticals with radionuclides. The process of functionalization using a bifunctional azacrown ligand is described, and the resulting conjugates are characterized by IR and Raman spectroscopy. Their complexes with <sup>207</sup>Bi show a high stability in medically relevant media, thus encouraging the further study of these conjugates in vivo as potential combined radiopharmaceuticals.



**Citation:** Khabirova, S.; Aleshin, G.; Plakhova, T.; Zubenko, A.; Shchukina, A.; Fedorova, O.; Averin, A.; Belova, E.; Bazarkina, E.; Kvashnina, K.; et al. CeO<sub>2</sub>-Azacrown Conjugate as a Nanoplatfor for Combined Radiopharmaceuticals. *Nanomaterials* **2022**, *12*, 4484. <https://doi.org/10.3390/nano12244484>

Academic Editors: Wan-Liang Lu and Alexandru Mihai Grumezescu

Received: 31 July 2022

Accepted: 16 December 2022

Published: 18 December 2022

**Publisher's Note:** MDPI stays neutral with regard to jurisdictional claims in published maps and institutional affiliations.



**Copyright:** © 2022 by the authors. Licensee MDPI, Basel, Switzerland. This article is an open access article distributed under the terms and conditions of the Creative Commons Attribution (CC BY) license (<https://creativecommons.org/licenses/by/4.0/>).

**Keywords:** nanoceria; surface functionalization; radiolabeled nanoparticles; bismuth; radiopharmaceuticals

## 1. Introduction

Diagnostics incorporating labeled nanoparticles (NPs) can be used for the early detection, characterization, and staging of diseases, as well as for effective radionuclide therapy [1]. The small size of nanoparticles allows them to pass through cell membranes and deliver the radiopharmaceutical closer to the nucleus of the tumor cell, thus reducing the effect of ionizing radiation on healthy organs and tissues [2]. In addition, nanoparticles are often effective vectors for drug delivery [3], whereby the pharmacokinetic and pharmacodynamic properties of the nanoparticles can be optimized by modifying their surface.

Cerium dioxide (or ceria) nanoparticles can be used for various biomedical purposes due to their unique properties. The toxicity of cerium dioxide nanoparticles has been studied previously both in vitro and in vivo [4]. It was shown that cerium dioxide nanoparticles stabilized by biocompatible surfactants (citric acid, dextran, PVP, polyacrylate, PEG) are not toxic to cells even in high concentrations [5,6]. Their biological activity results in antioxidant properties that can be applied as neuro- [7], cardio- [8,9] and radioprotectors [10], as well as anti-inflammatory drugs [11]. Moreover, ceria nanoparticles are capable of exhibiting either anti- or prooxidant properties, depending on the difference in pH levels in various subcellular regions [12]. CeO<sub>2</sub> can also act as an enzyme mimetic and enhance the action of natural enzymes [13,14]. The exact mechanism of the biological action of ceria is a subject of discussion [10,15], however, it has been shown that the antioxidant activity of CeO<sub>2</sub> nanoparticles is directly dependent on their size [16].

Cancer cells produce reactive oxygen species more actively than healthy cells due to the lack of redox control [17]. Prooxidant agents cause additional oxidative stress in cancer cells and lead to their apoptotic death [18]. Accordingly, CeO<sub>2</sub> nanoparticles are more cytotoxic for cancer cells, while the opposite is observed for healthy cells [19]. In addition,

due to its pH sensitivity, ceria exhibits vector properties and can target the delivery of radiopharmaceuticals to the affected tissue [20].

Previously, there have been several attempts of using CeO<sub>2</sub> nanoparticles for nuclear medicine for simultaneous diagnosis and radioprotection [21–23]. However, in terms of nuclear-physical characteristics, there are no isotopes of cerium that are optimal for diagnosis or therapy [24]. Ceria nanoparticles have also been used as a part of composite material for <sup>68</sup>Ge/<sup>68</sup>Ga generator for clinical uses [25]. Another approach for obtaining radionuclide-labeled nanoparticles is indirect conjugation using bifunctional chelators, which bind to the nanoparticle and then form a complex compound with the radionuclide [26]. Modifying the surface of these particles [27] with bifunctional chelators could open new perspectives and expand the number of radionuclides that can potentially be used.

Thus, the study of cerium dioxide conjugates and their complexes with radionuclides of other elements applicable in nuclear medicine is a promising direction for developing combined radiopharmaceuticals with novel properties. These nanoplatforms can then form complex compounds with radionuclides for both diagnostic and radionuclide therapy. The best approach for the latter is the use of alpha-emitters. Due to their relatively low range in the tissue and high linear energy transfer, they minimize damage to healthy organs and tissues [28]. Bismuth radionuclides <sup>212</sup>Bi (α, T<sub>1/2</sub> = 60.5 min) and <sup>213</sup>Bi (α, T<sub>1/2</sub> = 46 min) have attracted great interest due to their compatible nuclear properties, and some of their compounds have already shown promising results in clinical trials [29,30]. Thus, the conjugation of CeO<sub>2</sub> conjugates with alpha-emitting <sup>212</sup>Bi or <sup>213</sup>Bi could lead to a radiopharmaceutical for radionuclide therapy, which has a radioprotective effect for non-cancer cells.

The most widely used method of radioactive labelling is the modification of the particle surface with a multidentate bifunctional chelator (BFC) followed by the complexation with a radionuclide [26]. The selection of the BFC depends on the radionuclide, the synthesis strategy, physical properties, the desirable polarity and biodistribution properties. Previously, the NPs-azacrown ligand-radionuclide systems for application in radiopharmaceutical purposes have already been studied. For example, the authors of the article [31] tested AuNP modified by peptide-DOTA (1,4,7,10-tetraazacyclododecane-1,4,7,10-tetraacetic acid) conjugates for drug delivery in pancreatic and colon cancer cell lines. In vivo application of these functionalized nanoparticles with proper coating can improve the quality of PET images. Another study [32] reported the use of <sup>177</sup>Lu labelled conjugates of silica nanoparticles and DOTA for targeted radiation therapy in melanoma models. In addition, it was previously shown that azacrown ethers and their derivatives with the number of heteroatoms in the cycle 5 and 6 form stable complex compounds with many metal cations, including Bi<sup>3+</sup> [33]. Therefore, these macrocyclic ligands can be used as bifunctional chelators for bonding the radionuclide to nanoparticles.

To the best of our knowledge, this study presents the first ever report of the possibility of modifying ceria nanoparticles with a macrocyclic azacrown ligand for applications in radiopharmaceuticals. The macrocycle with a relatively large cavity (Figure 1) is chosen as the model object since its complexes with bismuth radionuclides have already demonstrated high in vitro and in vivo stability [33].

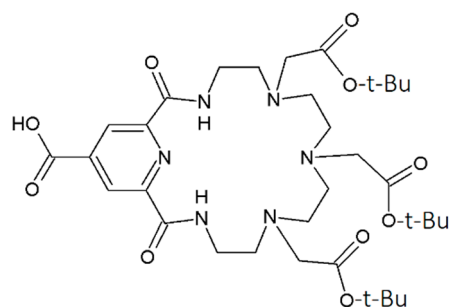


**Figure 1.** Structure of ligand L investigated in this study.

## 2. Experimental

### 2.1. Reagents

Solutions of cerium ammonium nitrate  $(\text{NH}_4)_2\text{Ce}(\text{NO}_3)_6$  (Sigma-Aldrich) were used as precursors for the synthesis of cerium dioxide nanoparticles. The chemicals used in this research were chemically pure 2-(chloromethyl)oxirane (ECH) as the linker, 2-(1H-benzotriazol-1-yl)-1,1,3,3-tetramethyluronium hexafluorophosphate (HBTU), aqueous solutions of NaOH and  $\text{NH}_3$ , triethylamine, dimethyl sulfoxide (DMSO), 85% formic acid solution, and deionized water (Milli-Q, 18 M $\Omega$ m). A solution of  $^{207}\text{Bi}]\text{Bi}^{3+}$  in HCl (0.9 MBq) as a labeling agent was purchased from JSC Ritverc.  $\text{Bi}(\text{ClO}_4)_3$  or  $\text{BiCl}_3$  solutions were used as a carrier for  $^{207}\text{Bi}$ . Azacrown ligand L (Figure 1) was prepared by a previously reported method [34].

### 2.2. Nanoceria Synthesis and Surface Functionalization

The functionalization of cerium oxide nanoparticles was carried out as follows. The method consisted of the consecutive synthesis of particles (Figure 2A) modified by the linker and ligand L (Figure 2E). Ceria nanoparticles were obtained by chemical deposition from 0.1 M of  $(\text{NH}_4)_2\text{Ce}(\text{NO}_3)_6$  by 3 M of  $\text{NH}_3 \cdot \text{H}_2\text{O}$  at room temperature and constant stirring for 24 h. As a result, a yellow precipitate of cerium dioxide was formed, which was subsequently decanted by centrifugation, washed with water twice, and dried. In the following stage, 50 mg of the as-prepared  $\text{CeO}_2$  yellow power was suspended in 2 mL of a 0.1 M NaOH solution for 5 min. Then, 1 mL of ECH was added, followed by the addition of 100  $\mu\text{L}$  of 2 M NaOH. The suspension was stirred at ambient conditions for 12 h. The reaction mixture was centrifuged, and the supernatant was decanted. The nanoparticles were washed with water then centrifuged until the pH value of the suspension reached 7. The resulting nanoparticles (1.1 equiv.) were added to a solution of ligand L (1 equiv.), HBTU (3.5 equiv.), and triethylamine (3.5 equiv.) in DMSO and stirred at room temperature for 12 h. Upon completion of the reaction, the precipitate was separated by centrifugation and washed with water. At the final stage, 85% formic acid solution was added and stirred for 3 h at room temperature to remove the tert-butyl protection of the carboxyl groups of the ligand L. The resulting materials were separated, washed with water, and dried.

### 2.3. Characterization of Modified Nanoparticles

*Electron microscopy:* The microstructures of the samples were studied by transmission electron microscopy (TEM) on a Zeiss Libra 200FE electron microscope. The analysis of interplanar spacings was carried out using electron diffraction data obtained during the TEM experiment. The size of particles was calculated by determining the average diameter of approximately 300 particles according to the TEM data.

*Spectroscopy method:* Infrared (IR) spectra were recorded at 25 °C on a Thermo Scientific Nicolet iS5 FT-IR spectrometer either in KBr or on the working surface of the internal reflectance attachment using a diamond optical element by attenuated total reflection (ATR). The spectral resolution was 4  $\text{cm}^{-1}$ . Raman spectra were obtained using a Renishaw inVia Raman spectrometer with a 50-mW laser diode at a wavelength of 633 nm. The spectral range was set between 100 and 3500  $\text{cm}^{-1}$ .

*Thermogravimetry:* The efficiency of ligand binding to the surface of  $\text{CeO}_2$  NPs was analyzed by thermogravimetric analysis (TGA). The measurements were carried out in an atmosphere of air using a Jupiter NETZSCH STA 449 F1 thermal analyzer combined with a quadrupole mass spectrometer NETZSCH QMS 403 C Aëolos, from 30 to 900 °C at a heating rate of 10 °C/min.

*$\zeta$ -potential determination:* The modification of the surface of nanoparticles at each stage was confirmed by determining the isoelectric point from a series of  $\zeta$ -potential measurements at different pH values in the range 2–11. The pH values of a series of samples in 0.01 M  $\text{NaClO}_4$  were established by adding various concentrations of NaOH or  $\text{HClO}_4$  solutions. The  $\zeta$ -potential was assessed by dynamic light scattering on a Malvern ZETASIZER nano-ZS instrument.

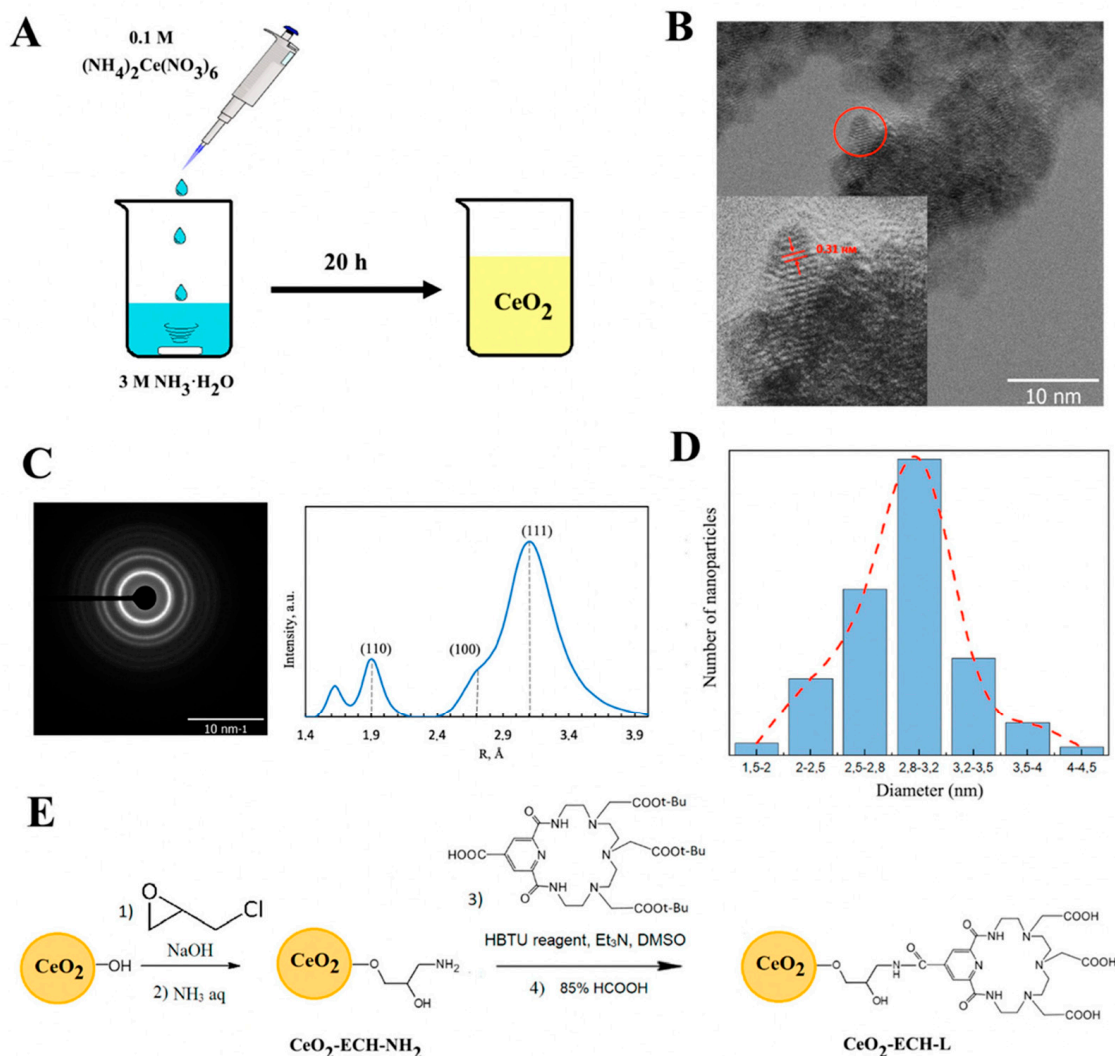


**Figure 2.** (A) Synthesis of CeO<sub>2</sub> NPs by chemical deposition. (B) TEM image of the CeO<sub>2</sub> surface (scale bar = 10 nm). The inset shows a high-resolution TEM image of the as-prepared CeO<sub>2</sub> NPs. (C) Selected area electron diffraction (SAED) data. (D) CeO<sub>2</sub> NPs size distribution according to TEM data. (E) Schematic showing the modification of cerium nanoparticles with azacrown ether L through the ECH linker.

*X-ray absorption spectroscopy:* HERFD-XANES experiments were performed at BM20 beamline of the European Synchrotron Radiation Facility, Grenoble (France) [35]. The incident energy was selected using the (111) reflection from a double crystal Si monochromator. Rejection of higher harmonics was achieved by two Rh mirrors working at an angle of 2.5 mrad relative to the incident beam. HERFD-XAS spectra were measured using an X-ray emission spectrometer [36] at 90° horizontal scattering angle. Sample, analyzer crystal and Si detector (Ketek) were arranged in a vertical Rowland geometry. The Ce HERFD-XAS spectra at the L<sub>3</sub> edge were obtained by recording the maximum intensity of the Ce Lα<sub>1</sub> emission line (4839 eV) as a function of the incident energy. The emission energy was selected using the (331) reflection of five spherically bent Ge crystal analyzers (with R = 1 m) aligned at an 80.7° Bragg angle. The vertical size of the beam at the sample, which defines the energy resolution, was 80 μm. A combined (incident convoluted with emitted) energy resolution of 1.2 eV was obtained, as determined by measuring the FWHM of the elastic peak. Samples for the HERFD-XANES measurements were prepared as wet pastes and sealed with single kapton confinement (of 25 mm thickness).

#### 2.4. Stability in Buffer Solutions

The conjugates of CeO<sub>2</sub> with ligand L (CeO<sub>2</sub>-ECH-L) were complexed with a solution of [<sup>207</sup>Bi]BiCl<sub>3</sub> as a long-lived analogue of medically applicable <sup>212</sup>Bi and <sup>213</sup>Bi. The stability of the resulting complex CeO<sub>2</sub>-ECH-L-<sup>207</sup>Bi was studied in the following media: 0.9% NaCl, phosphate-buffered saline (PBS) with a pH of 7.4, 0.05 M 4-(2-hydroxyethyl)-1-piperazineethanesulfonic acid (HEPES) and in the fetal bovine serum 1:1 (FBS) (HyClone). Complexes with a solid phase concentration of 10<sup>-3</sup> g·l<sup>-1</sup> and a [<sup>207</sup>Bi]Bi<sup>3+</sup> concentration of 10<sup>-9</sup> M were prepared in solutions of 0.9% NaCl by the addition of ammonium acetate buffer solution (0.1 M) to fix the pH in the range 6.5–7.2, and in PBS, HEPES or FBS. All samples were incubated at 37 °C and continuously stirred. The labeled CeO<sub>2</sub>-<sup>207</sup>Bi and CeO<sub>2</sub>-ECH-L-<sup>207</sup>Bi were extracted from the mixture by solid–liquid separation behaviors in centrifugal sedimentation. Aliquots of the supernatant were sampled and analyzed using gamma spectrometry.

### 3. Results and Discussion

#### 3.1. Synthesis and Functionalization of CeO<sub>2</sub> Nanoparticles

A schematic of the synthesis of cerium dioxide nanoparticles is given in Figure 2A. According to TEM data (Figure 2B), spherical crystalline nanoparticles were formed using the synthesis procedure. The insert in Figure 2B demonstrates a high-resolution micrograph showing lattice bands of strongly crystallized particles with a distance of 0.31 nm, which corresponds to the (111) plane of CeO<sub>2</sub> nanoparticles. The electron diffraction (ED) results obtained during the microscopic investigation show that only diffraction reflections corresponding to the CeO<sub>2</sub> fluorite structure are observed (Figure 2C). The diameter of the particles is 2.9 nm according to the analysis of TEM data (Figure 2D).

The functionalization of CeO<sub>2</sub> nanoparticles was conducted according to the scheme in Figure 2E. Typical TEM images and particle size distribution of the surface-modified nanocerium are shown in Figure S1 in the Supplementary Information. The average diameter of CeO<sub>2</sub>-ECH-L is 2.8 nm with a standard deviation of 0.2 nm. Nanoparticles of the obtained conjugates had a hydrodynamic size of 10–17 nm according to DLS results (see Figure S2 in the Supplementary Information). This size did not change in buffer solutions (HEPES and PBS) as well as in saline.

The prepared nanoparticles were pre-modified with epichlorohydrin (ECH) to further obtain a hydrophilic surface coated with amino groups. At the next stage, ligand functionalization was carried out through an unprotected carboxyl group by the method of peptide synthesis, followed by the removal of tert-butyl protective groups to obtain the CeO<sub>2</sub>-ECH-L conjugate. Infrared (Figure 3A) and Raman (Figure 3B,C) spectroscopy was used to determine the structure and composition of the materials and functionalization effectiveness. The deformation Ce–O bands (845, 940, 1060, 1330 cm<sup>-1</sup>) are observed in the IR spectra for all samples. Vibrations of R-NH<sub>2</sub> groups in the region of 1100 cm<sup>-1</sup> confirm the formation of the CeO<sub>2</sub>-ECH-NH<sub>2</sub> structure. After ligand L functionalization, peaks characteristic of the amino group (3500–3300, 1110 cm<sup>-1</sup>), the formed secondary amide (1694 cm<sup>-1</sup>), vibrations in the pyridine ring (1567–1557, 778 cm<sup>-1</sup>), and carboxyl groups (1425, 1403 cm<sup>-1</sup>) of the organic molecules are traced (Figure 3A).

A clear difference between the analyzed samples can be observed by Raman spectroscopy. Figure 3B shows the Raman spectra of the synthesized functionalized CeO<sub>2</sub> nanoparticles. The spectra were recorded at minimum laser intensities (50 mW) to avoid a possible degradation effect of the samples. The first order of the CeO<sub>2</sub> Raman spectrum is characterized by the presence of a F<sub>2g</sub> vibrational mode at approximately 465 cm<sup>-1</sup>, associated with the elongation of the Ce–O bond, where Ce and O are coordinated at eight and four times, respectively. The weak band observed at 1050 cm<sup>-1</sup> may be related to the asymmetry of the primary A<sub>1g</sub> mode, combined with small additional contributions of E<sub>g</sub> and F<sub>2g</sub> symmetries. The presence of a band in the modified CeO<sub>2</sub> samples at approximately 600 cm<sup>-1</sup> can be observed, which may be related to the presence of Ce<sup>3+</sup> on the surface of the solid, promoting a non-stoichiometric condition and the appearance of



this band at  $600\text{ cm}^{-1}$ . Moreover, the presence of bond vibrations in the Raman spectra of organic molecules confirms the change in the structure of the surface of cerium dioxide nanoparticles [37,38].

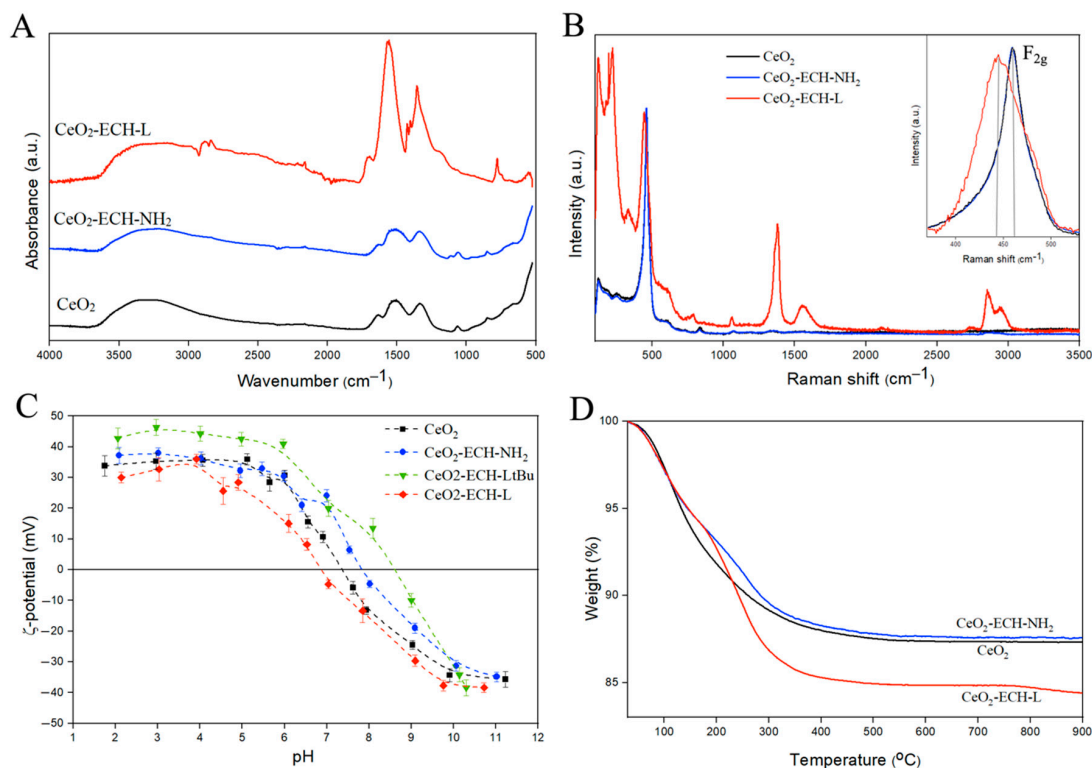


**Figure 3.** (A) IR spectra of the initial CeO<sub>2</sub> and synthesized functionalized CeO<sub>2</sub> nanoparticles. (B) Raman spectra obtained from samples of the initial CeO<sub>2</sub> and modified series. The inset shows enlarged Raman spectra, where the change in the position of the F<sub>2g</sub> peak ( $465\text{ cm}^{-1}$ ) of the modified samples relative to the comparison sample CeO<sub>2</sub> is observed. (C) Dependence of the zeta potential on the pH value ( $I = 0.01\text{ M}$ ). (D) weight loss curves obtained from thermogravimetric analysis.

The bands in the Raman spectra can shift with changes on the surface of the crystal [39]. The change in the half-width at half-maximum and the shift of the maximum peak at  $465\text{ cm}^{-1}$  (F<sub>2g</sub>) of the modified series of particles relative to the initial CeO<sub>2</sub> are shown in Figure 3C. Based on the above observation, the surface of the nanoparticles has changed, which confirms the change in the structure of the substances.

The modification of the surface of nanoparticles at each stage was confirmed by a series of  $\zeta$ -potential measurements at different pH values, as shown in Figure 3D. The functionalization of particles by amino groups on the CeO<sub>2</sub> surface show a shift of the isoelectric point in the region with a high pH value ( $\text{pI} = 7.4$ ). The shift of the isoelectric point to the left for CeO<sub>2</sub>-ECH-L-tBu ( $\text{pI} = 6.8$ ) is explained by the presence of carboxyl groups in the ligand structure, which are deprotonated with increasing pH value, forming a negative charge on the surface. At the same time, nitrogen atoms in the macrocyclic and pyridine fragments of the ligands also affect the pI position. They shift the isoelectric point to the region with low pH values due to their basic properties. Thus, from a combination of IR and Raman spectroscopy and  $\zeta$ -potential results, we can conclude that CeO<sub>2</sub> nanoparticles were functionalized with azacrown ether L.

The effectiveness of ligand binding to the surface of ceria nanoparticles was evaluated using the method of thermogravimetric analysis combined with mass spectrometry (TGA-MS) in an atmosphere of air (Figure 3D). Weight loss occurs smoothly in the range from  $30\text{ }^{\circ}\text{C}$  to  $400\text{ }^{\circ}\text{C}$ . The weight loss for CeO<sub>2</sub>-ECH-L is greater compared to CeO<sub>2</sub>, which is a consequence of ligand presence on the surface. In addition, there is a change in the tilt angle of the lines of the modified sample at the beginning of heating caused by the

oxidation of the organic part of the material. The TGA spectra of the free ligand are shown in Figure S3 in the Supplementary Information. According to the TGA-MS results, the release of water for CeO<sub>2</sub> and CeO<sub>2</sub>-ECH-NH<sub>2</sub> NPs begins from the moment of heating and ends at temperatures up to 200 °C due to the presence of a substantial amount of water on the surface of the sample (see Figure S4 in the Supplementary Information). For conjugation of the nanoparticles and ligand L, water is released when heated to 400 °C due to the oxidation of the organic molecules on the particles. The insignificant amount of CO<sub>2</sub> registered for CeO<sub>2</sub> is related to experimental conditions during particle synthesis. In other cases, the CO<sub>2</sub> peak in the mass spectra confirms the presence of organic molecules on the CeO<sub>2</sub> surface.

Figure 4 shows the HERFD-XANES data for the investigated samples. CeO<sub>2</sub> (NIST) was used as a standard with a cell parameter of 5.4117 Å and a particle size of more than 25 nm.

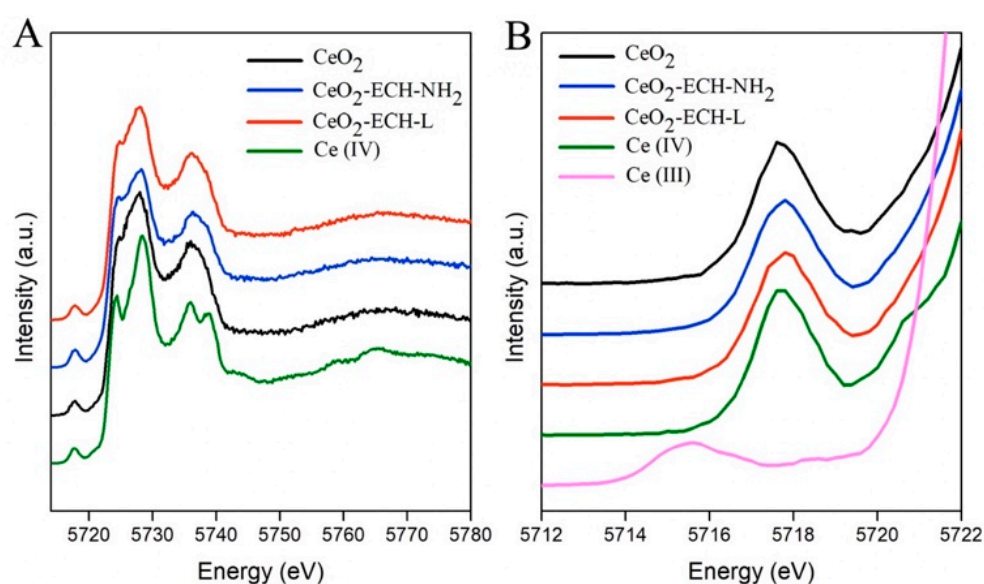


**Figure 4.** (A) Ce L<sub>3</sub> edge HERFD-XANES data for CeO<sub>2</sub> nanoparticles before and after surface modification, compared to CeO<sub>2</sub> and Ce<sub>2</sub>(SO<sub>4</sub>)<sub>3</sub>, as Ce(IV) and Ce(III) references, respectively. (B) Enlarged pre-edge region.

The HERFD-XANES spectra reveal the presence of the dipole-allowed 2p-5d transitions (main edge transitions in the energy range 5723–5730 eV) and of the dipole forbidden but quadrupole-allowed 2p-4f transitions (at the pre-edge in the energy range 5715–5720 eV) [40,41]. The spectra of the studied samples relative to the standard in the main edge region have a smoother shape due to the size effect. This effect was discussed earlier by Plakhova et al. [15]. The presence of Ce (III) would lead to the appearance of an additional peak in the pre-edge (~5715.5 eV) due to an increase in the number of electrons and electron–electron interactions on the 4f orbital. The shape and position of the pre-edge peaks (~5717.8 eV) of our CeO<sub>2</sub> samples before and after the modification process corresponds to the Ce (IV) standard (Figure 4B). Thus, the modification of the CeO<sub>2</sub> surface with azacrown ether ligand does not change the cerium oxidation state in nanoparticles, despite the use of reducing agents in the synthesis procedure.

### 3.2. Stability in Buffer Solutions

The stability of the CeO<sub>2</sub>-ECH-L-<sup>207</sup>Bi nanoplatfrom and the extent of bismuth absorption on the surface of nanoparticles were studied in 0.9% NaCl with ammonium acetate buffer solution, PBS with pH = 7.4, and HEPES (pH 7.1). Dissociation of the complex under these conditions is a highly probable process due to the large number of competing ions

capable of re-chelating radionuclide cations. This experiment can partially simulate the behavior of a potential radiopharmaceutical when it is injected into a living organism.

Figure 5A–C shows the labeling efficiency at different time intervals of equilibration under constant stirring and at a temperature of 37 °C. In Figure 5A,B, the conjugate of the nanoparticles and ligand bonds with the radionuclide  $^{207}\text{Bi}$  over 90% after 30 min of mixing, and after 4 h the radiolabeling yield is quantitative. The formation of nanoparticle-ligand-radionuclide structures is relatively slow, which could be due to the presence of competing ions in the solution. Moreover, as a result of re-chelation of  $[\text{}^{207}\text{Bi}]\text{Bi}^{3+}$  in the solution, the radiolabeling yield does not exceed 80% in this biological media.

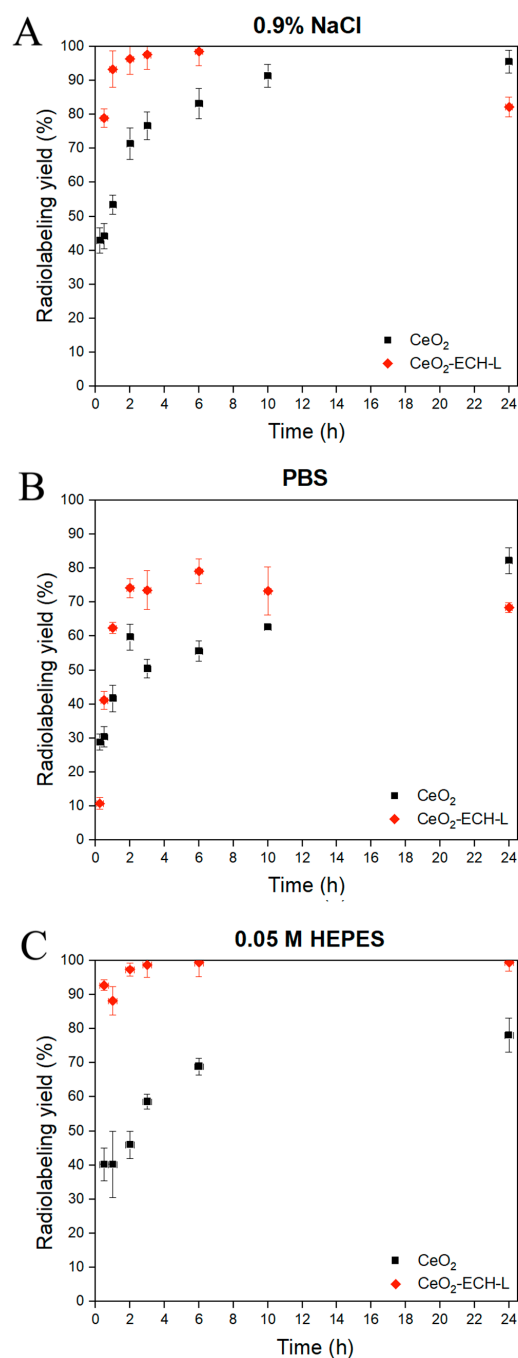


**Figure 5.** Kinetic stability of complexes  $\text{CeO}_2\text{-}^{207}\text{Bi}$  and  $\text{CeO}_2\text{-ECH-L-}^{207}\text{Bi}$  in buffer solutions: (A) 0.9 % NaCl with ammonium acetate buffer solution (pH = 6.8); (B) PBS (pH = 7.4); (C) 0.05 M HEPES (pH = 7.1).



As shown in Figure 5C,  $[^{207}\text{Bi}]\text{Bi}^{3+}$  binds rapidly to the ligand L on the surface of the nanoceria in 0.05 M HEPES, and after 30 min, the radiolabeling yield exceeds 90%. During the day, the complex  $\text{CeO}_2\text{-ECH-L-}^{207}\text{Bi}$  does not dissociate and the yield is c.a. 99% after 24 h. At the same time, the absorption of bismuth cations on  $\text{CeO}_2$  reaches 75% after 24 h, however, this process exhibits slow kinetics compared with the formation of the complex. This fact can be explained by the absence of re-chelating agents in the buffer. The high kinetic stability of the conjugate of nanoparticles and the ligand L with radionuclide  $^{207}\text{Bi}$  is obtained in HEPES, which makes it possible to use this system for in vivo experiments.

The stability of the  $\text{CeO}_2\text{-ECH-L-}^{207}\text{Bi}$  was analyzed in the FBS. This experiment can partially simulate the behavior of a potential radiopharmaceutical when it is introduced into a living organism and then circulated in the blood. As shown in Figure 6, the radiolabeling yield does not exceed 30% after 24 h for  $\text{CeO}_2\text{-ECH-L-}^{207}\text{Bi}$ . Dissociation of the complex under these conditions is a highly probable process due to the large number of serum proteins that are able to re-chelate radionuclide cations.

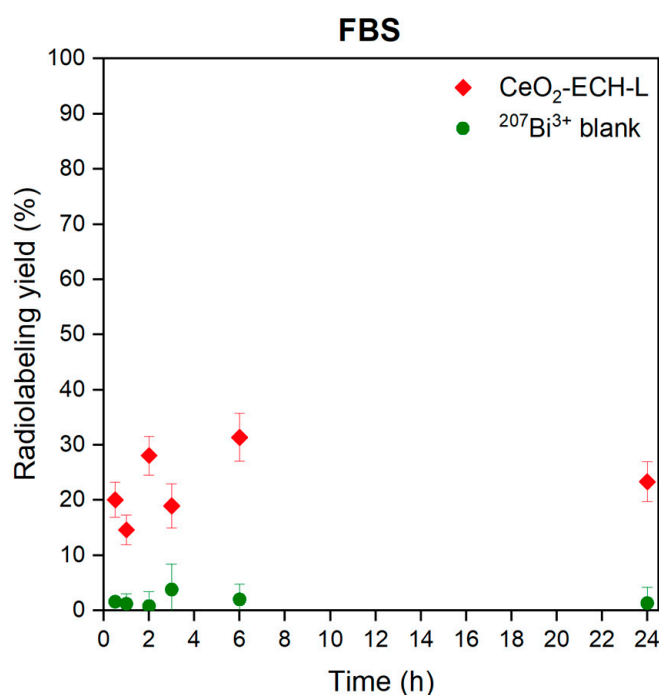


**Figure 6.** Dependencies characterizing the kinetic stability of  $\text{CeO}_2\text{-ECH-L-}^{207}\text{Bi}$  and  $^{207}\text{Bi}^{3+}$  in fetal bovine serum (FBS) in a ratio of 1:1.

We can conclude that the results of kinetic stability in FBS during the day for  $\text{CeO}_2\text{-ECH-L-}^{207}\text{Bi}$  are significantly lower than acceptable values for radiopharmaceuticals. On the other hand, the conjugate  $\text{CeO}_2\text{-EPC-L}$  can potentially be used for labelling with other radionuclides that demonstrate the stability of complexes under in vitro and in vivo conditions.

#### 4. Conclusions

This study proved that  $\text{CeO}_2$  nanoparticles are promising nanoagents in nuclear medicine. The functionalization of nanoceria by a macrocyclic azacrown ligand with six heteroatoms in the cavity and three pendant carboxylic arms is shown. The resulting conjugate forms a radiolabeled complex with  $^{207}\text{Bi}^{3+}$ , which is stable in saline and HEPES solutions but dissociates in FBS. These results are promising for further studies of the possible applications of this conjugate as a radiopharmaceutical. Moreover, we believe that the proposed method of conjugation can be extended to other azacrown ethers and  $\text{CeO}_2\text{-ECH-L}$  conjugate can be used as a multipurpose nanoplatform with various radionuclides for molecular imaging, therapy and theranostics of oncological diseases.

**Supplementary Materials:** The following supporting information can be downloaded at: <https://www.mdpi.com/article/10.3390/nano12244484/s1>, Figure S1: TEM image of the CeO<sub>2</sub>-ECH-L surface (scale bar = 50 nm) and CeO<sub>2</sub>-ECH-L size distribution according to TEM data; Figure S2: CeO<sub>2</sub>-ECH-L size distribution in the different buffer solutions according to DLS data; Figure S3: Curves obtained from thermogravimetric analysis of the CeO<sub>2</sub> and synthesized functionalized CeO<sub>2</sub> nanoparticles; Figure S4: TGA-MS results of initial (A) and surface-modified CeO<sub>2</sub> nanoparticles (B,C) obtained for the mass numbers 18 (H<sub>2</sub>O) and 44 (CO<sub>2</sub>).

**Author Contributions:** S.K.(Sofia Khabirova) and G.A. performed synthesis and modification of nanoparticles, radiolabelling of experiments and IR measurements, data analysis, preparation of the original manuscript. T.P. contributed to characterization and analysis of modified ceria nanoparticles. A.Z., A.S. and O.F. synthesized the macrocyclic bifunctional ligand. A.A. performed Raman spectroscopy. E.B. (Ekaterina Belova) performed TG-MS measurements. E.B. (Elena Bazarkina), K.K. and T.P. carried out HERFD-XANES experiments. G.A. and Stepan Kalmykov were involved in planning and supervision of the work. T.P., K.K. and S.K.(Stepan Kalmykov) edited the original draft. All authors have read and agreed to the published version of the manuscript.

**Funding:** This study was supported by the Russian Science Foundation, project No. 21-73-00101, <https://rscf.ru/project/21-73-00101/>, accessed on 29 July 2021. S.K. acknowledge support by the Russian Ministry of Science and Education under grant No. 075-15-2022-1107. K.O.K. and E.F.B. acknowledge support from the European Research Council under grant agreement 759696.

**Data Availability Statement:** Not applicable.

**Acknowledgments:** The authors would like to thank E. O. Anokhin and D. A. Kozlov for TEM studies of the samples. Authors thank HZDR for the beamtime allocation at the Rossendorf Beamline of ESRF and ID26 beamline of ESRF for providing Ge crystal for the Ce L3 HERFD-XANES measurements.

**Conflicts of Interest:** The authors declare no conflict of interest.

## References

1. Goel, S.; England, C.G.; Chen, F.; Cai, W. Positron Emission Tomography and Nanotechnology: A Dynamic Duo for Cancer Theranostics. *Adv. Drug Deliv. Rev.* **2017**, *113*, 157–176. [[CrossRef](#)]
2. Chou, L.Y.T.; Ming, K.; Chan, W.C.W. Strategies for the Intracellular Delivery of Nanoparticles. *Chem. Soc. Rev.* **2011**, *40*, 233–245. [[CrossRef](#)] [[PubMed](#)]
3. Ge, J.; Zhang, Q.; Zeng, J.; Gu, Z.; Gao, M. Radiolabeling Nanomaterials for Multimodality Imaging: New Insights into Nuclear Medicine and Cancer Diagnosis. *Biomaterials* **2020**, *228*, 119553. [[CrossRef](#)] [[PubMed](#)]
4. Casals, E.; Zeng, M.; Parra-Robert, M.; Fernández-Varo, G.; Morales-Ruiz, M.; Jiménez, W.; Puentes, V.; Casals, G. Cerium Oxide Nanoparticles: Advances in Biodistribution, Toxicity, and Preclinical Exploration. *Small* **2020**, *16*, 1254–1261. [[CrossRef](#)] [[PubMed](#)]
5. Hirst, S.M.; Karakoti, A.; Singh, S.; Self, W.; Tyler, R.; Seal, S.; Reilly, C.M. Bio-Distribution and in Vivo Antioxidant Effects of Cerium Oxide Nanoparticles in Mice. *Environ. Toxicol.* **2013**, *28*, 107–118. [[CrossRef](#)] [[PubMed](#)]
6. Heckman, K.L.; Estevez, A.Y.; DeCoteau, W.; Vangellow, S.; Ribeiro, S.; Chiarenzelli, J.; Hays-Erlichman, B.; Erlichman, J.S. Variable in Vivo and in Vitro Biological Effects of Cerium Oxide Nanoparticle Formulations. *Front. Pharmacol.* **2020**, *10*, 1599. [[CrossRef](#)]
7. An, Z.; Yan, J.; Zhang, Y.; Pei, R. Applications of Nanomaterials for Scavenging Reactive Oxygen Species in the Treatment of Central Nervous System Diseases. *J. Mater. Chem. B* **2020**, *8*, 8748–8767. [[CrossRef](#)]
8. Niu, J.; Azfer, A.; Rogers, L.M.; Wang, X.; Kolattukudy, P.E. Cardioprotective Effects of Cerium Oxide Nanoparticles in a Transgenic Murine Model of Cardiomyopathy. *Cardiovasc. Res.* **2007**, *73*, 549–559. [[CrossRef](#)]
9. Celardo, I.; Pedersen, J.Z.; Traversa, E.; Ghibelli, L. Pharmacological Potential of Cerium Oxide Nanoparticles. *Nanoscale* **2011**, *3*, 1411–1420. [[CrossRef](#)]
10. Popov, A.L.; Zaichkina, S.I.; Popova, N.R.; Rozanova, O.M.; Romanchenko, S.P.; Ivanova, O.S.; Smirnov, A.A.; Mironova, E.V.; Selezneva, I.I.; Ivanov, V.K. Radioprotective Effects of Ultra-Small Citrate-Stabilized Cerium Oxide Nanoparticles in Vitro and in Vivo. *RSC Adv.* **2016**, *6*, 106141–106149. [[CrossRef](#)]
11. Wu, Y.; Ta, H.T. Different Approaches to Synthesising Cerium Oxide Nanoparticles and Their Corresponding Physical Characteristics, and ROS Scavenging and Anti-Inflammatory Capabilities. *J. Mater. Chem. B* **2021**, *9*, 7291–7301. [[CrossRef](#)] [[PubMed](#)]
12. Datta, A.; Mishra, S.; Manna, K.; Das Saha, K.; Mukherjee, S.; Roy, S. Pro-Oxidant Therapeutic Activities of Cerium Oxide Nanoparticles in Colorectal Carcinoma Cells. *ACS Omega* **2020**, *5*, 9714–9723. [[CrossRef](#)] [[PubMed](#)]
13. Pirmohamed, T.; Dowding, J.M.; Singh, S.; Wasserman, B.; Heckert, E.; Karakoti, A.S.; King, J.E.S.; Seal, S.; Self, W.T. Nanoceria Exhibit Redox State-Dependent Catalase Mimetic Activity. *Chem. Commun.* **2010**, *46*, 2736–2738. [[CrossRef](#)]
14. Singh, K.R.B.; Nayak, V.; Sarkar, T.; Singh, R.P. Cerium Oxide Nanoparticles: Properties, Biosynthesis and Biomedical Application. *RSC Adv.* **2020**, *10*, 27194–27214. [[CrossRef](#)] [[PubMed](#)]

15. Plakhova, T.V.; Romanchuk, A.Y.; Butorin, S.M.; Konyukhova, A.D.; Egorov, A.V.; Shiryayev, A.A.; Baranchikov, A.E.; Dorovatovskii, P.V.; Huthwelker, T.; Gerber, E.; et al. Towards the Surface Hydroxyl Species in CeO<sub>2</sub> Nanoparticles. *Nanoscale* **2019**, *11*, 18142–18149. [CrossRef] [PubMed]
16. Deshpande, S.; Patil, S.; Kuchibhatla, S.V.; Seal, S. Size Dependency Variation in Lattice Parameter and Valency States in Nanocrystalline Cerium Oxide. *Appl. Phys. Lett.* **2005**, *87*, 133113. [CrossRef]
17. Wang, J.; Luo, B.; Li, X.; Lu, W.; Yang, J.; Hu, Y.; Huang, P.; Wen, S. Inhibition of Cancer Growth in Vitro and in Vivo by a Novel ROS-Modulating Agent with Ability to Eliminate Stem-like Cancer Cells. *Cell Death Dis.* **2017**, *8*, e2887. [CrossRef]
18. Stone, W.L.; Krishnan, K.; Campbell, S.E.; Palau, V.E. The Role of Antioxidants and Pro-Oxidants in Colon Cancer. *World J. Gastrointest. Oncol.* **2014**, *6*, 55. [CrossRef]
19. Damle, M.A.; Shetty, V.G.; Jakhade, A.P.; Kaul-Ghanekar, R.; Chikate, R.C. Bi-Functional Nature of Nanoceria: Pro-Drug and Drug-Carrier Potentiality towards Receptor-Mediated Targeting of Doxorubicin. *New J. Chem.* **2020**, *44*, 17013–17026. [CrossRef]
20. Shcherbakov, A.B.; Zholobak, N.M.; Spivak, N.Y.; Ivanov, V.K. Advances and Prospects of Using Nanocrystalline Ceria in Cancer Theranostics. *Russ. J. Inorg. Chem.* **2014**, *59*, 1556–1575. [CrossRef]
21. Paquin, F.; Rivnay, J.; Salleo, A.; Stingelin, N.; Silva, C. Multi-Phase Semicrystalline Microstructures Drive Exciton Dissociation in Neat Plastic Semiconductors. *J. Mater. Chem. C* **2015**, *3*, 10715–10722. [CrossRef]
22. Bakht, M.K.; Sadeghi, M.; Tenreiro, C. A Novel Technique for Simultaneous Diagnosis and Radioprotection by Radioactive Cerium Oxide Nanoparticles: Study of Cyclotron Production of <sup>137m</sup>Ce. *J. Radioanal. Nucl. Chem.* **2012**, *292*, 53–59. [CrossRef]
23. Bakht, M.K.; Hosseini, V.; Honarpisheh, H. Radiolabeled Nanoceria Probes May Reduce Oxidative Damages and Risk of Cancer: A Hypothesis for Radioisotope-Based Imaging Procedures. *Med. Hypotheses* **2013**, *81*, 1164–1168. [CrossRef] [PubMed]
24. Nuclear Structure and Decay Data. Available online: <https://nds.iaea.org/relnsd/vcharthtml/VChartHTML.html> (accessed on 28 June 2022).
25. Chakravarty, R.; Shukla, R.; Ram, R.; Venkatesh, M.; Dash, A.; Tyagi, A.K. Nanoceria-PAN Composite-Based Advanced Sorbent Material: A Major Step Forward in the Field of Clinical-Grade <sup>68</sup>Ge/<sup>68</sup>Ga Generator. *ACS Appl. Mater. Interfaces* **2010**, *2*, 2069–2075. [CrossRef] [PubMed]
26. Enrique, M.A.; Mariana, O.R.; Mirshojaei, S.F.; Ahmadi, A. Multifunctional Radiolabeled Nanoparticles: Strategies and Novel Classification of Radiopharmaceuticals for Cancer Treatment. *J. Drug Target.* **2015**, *23*, 191–201. [CrossRef]
27. Patil, S.; Reshetnikov, S.; Haldar, M.K.; Seal, S.; Mallik, S. Surface-Derivatized Nanoceria with Human Carbonic Anhydrase II Inhibitors and Fluorophores: A Potential Drug Delivery Device. *J. Phys. Chem. C* **2007**, *111*, 8437–8442. [CrossRef]
28. Milenic, D.E.; Garmestani, K.; Brady, E.D.; Albert, P.S.; Ma, D.; Abdulla, A.; Brechbiel, M.W.  $\alpha$ -Particle Radioimmunotherapy of Disseminated Peritoneal Disease Using a <sup>212</sup>Pb-Labeled Radioimmunoconjugate Targeting HER2. *Cancer Biother. Radiopharm.* **2005**, *20*, 557–568. [CrossRef]
29. Rosenblat, T.L.; McDevitt, M.R.; Mulford, D.A.; Pandit-Taskar, N.; Divgi, C.R.; Panageas, K.S.; Heaney, M.L.; Chanel, S.; Morgenstern, A.; Sgouros, G.; et al. Sequential Cytarabine and  $\alpha$ -Particle Immunotherapy with Bismuth-213–Lintuzumab (HuM195) for Acute Myeloid Leukemia. *Clin. Cancer Res.* **2010**, *16*, 5303–5311. [CrossRef]
30. Autenrieth, M.E.; Seidl, C.; Bruchertseifer, F.; Horn, T.; Kurtz, F.; Feuerecker, B.; D'Alessandria, C.; Pfob, C.; Nekolla, S.; Apostolidis, C.; et al. Treatment of Carcinoma in Situ of the Urinary Bladder with an Alpha-Emitter Immunoconjugate Targeting the Epidermal Growth Factor Receptor: A Pilot Study. *Eur. J. Nucl. Med. Mol. Imaging* **2018**, *45*, 1364–1371. [CrossRef]
31. Chilug, L.E.; Leonte, R.A.; Patrascu, M.E.B.; Ion, A.C.; Tuta, C.S.; Raicu, A.; Manda, G.; Niculae, D. In Vitro Binding Kinetics Study of Gold Nanoparticles Functionalized with <sup>68</sup>Ga-DOTA Conjugated Peptides. *J. Radioanal. Nucl. Chem.* **2017**, *311*, 1485–1493. [CrossRef]
32. Zhang, X.; Chen, F.; Turker, M.Z.; Ma, K.; Zanzonico, P.; Gallazzi, F.; Shah, M.A.; Prater, A.R.; Wiesner, U.; Bradbury, M.S.; et al. Targeted Melanoma Radiotherapy Using Ultrasmall <sup>177</sup>Lu-Labeled  $\alpha$ -Melanocyte Stimulating Hormone-Functionalized Core-Shell Silica Nanoparticles. *Biomaterials* **2020**, *241*, 119858. [CrossRef] [PubMed]
33. Egorova, B.V.; Matazova, E.V.; Mitrofanov, A.A.; Yu, A.G.; Trigub, A.L.; Zubenko, A.D.; Fedorova, O.A.; Fedorov, F.Y.; Kalmykov, S.N. Novel Pyridine-Containing Azacrownethers for the Chelation of Therapeutic Bismuth Radioisotopes: Complexation Study, Radiolabeling, Serum Stability and Biodistribution. *Nucl. Med. Biol.* **2018**, *60*, 1–10. [CrossRef] [PubMed]
34. Zubenko, A.D.; Shchukina, A.A.; Fedorova, O.A. Synthetic Approaches to the Bifunctional Chelators for Radionuclides Based on Pyridine-Containing Azacrown Compounds. *Synthesis* **2019**, *51*, 1087–1095. [CrossRef]
35. Scheinost, A.C.; Claussner, J.; Exner, J.; Feig, M.; Findeisen, S.; Hennig, C.; Kvashnina, K.O.; Naudet, D.; Prieur, D.; Rossberg, A.; et al. ROBL-II at ESRF: A Synchrotron Toolbox for Actinide Research. *J. Synchrotron Radiat.* **2021**, *28*, 333–349. [CrossRef] [PubMed]
36. Kvashnina, K.O.; Scheinost, A.C. A Johann-Type X-Ray Emission Spectrometer at the Rossendorf Beamline. *J. Synchrotron Radiat.* **2016**, *23*, 836–841. [CrossRef] [PubMed]
37. Schilling, C.; Hofmann, A.; Hess, C.; Ganduglia-Pirovano, M.V. Raman Spectra of Polycrystalline CeO<sub>2</sub>: A Density Functional Theory Study. *J. Phys. Chem. C* **2017**, *121*, 20834–20849. [CrossRef]
38. Hernández, W.Y.; Laguna, O.H.; Centeno, M.A.; Odriozola, J.A. Structural and Catalytic Properties of Lanthanide (La, Eu, Gd) Doped Ceria. *J. Solid State Chem.* **2011**, *184*, 3014–3020. [CrossRef]

39. Fasolato, C.; Domenici, F.; Sennato, S.; Mura, F.; De Angelis, L.; Luongo, F.; Costantini, F.; Bordini, F.; Postorino, P. Dimensional Scale Effects on Surface Enhanced Raman Scattering Efficiency of Self-Assembled Silver Nanoparticle Clusters. *Appl. Phys. Lett.* **2014**, *105*, 073105. [[CrossRef](#)]
40. Kvashnina, K.O.; Butorin, S.M.; Glatzel, P. Direct Study of the f-Electron Configuration in Lanthanide Systems. *J. Anal. At. Spectrom.* **2011**, *26*, 1265–1272. [[CrossRef](#)]
41. Zaslavov, P.; Amidani, L.; Retegan, M.; Walter, O.; Caciuffo, R.; Kvashnina, K.O. HERFD-XANES and RIXS Study on the Electronic Structure of Trivalent Lanthanides across a Series of Isostructural Compounds. *Inorg. Chem.* **2022**, *61*, 1817–1830. [[CrossRef](#)]